Environmental Science & Technology

pubs.acs.org/est

Article

Single-Cell/Molecule Energetic Elucidation of Shuttle-Enhanced Extracellular Electron Transfer: Implications for Iron and Phosphorus Mobilization

Yuke Fan,[#] Jialin Chi,[#] Liping Fang, Chonghao Jia, Yi Zhang, Kai Liu, Yundang Wu, Xiaokun Li, Jianwei Lu, Christine V. Putnis, Andreas Kappler, Wenjun Zhang,* Fangbai Li,* and Lijun Wang

Cite This: *Environ. Sci. Technol.* 2026, 60, 13414−13426

Read Online

ACCESS | Metrics & More | Article Recommendations | Supporting Information

ABSTRACT: Electron shuttles (ESs) critically enhance microbial extracellular electron transfer (EET), a key biogeochemical process that drives iron cycling and the activation of nutrients like phosphorus. However, existing studies are largely qualitative, focusing on EET pathway identification or current density measurements without quantitatively resolving the underlying energetics. Here, we establish an atomic force microscopy-based single-cell and single-molecule force spectroscopy platform, enabling the first direct quantification of microbial-ES-mineral interfacial energies. We find that riboflavin amplifies the adhesion energy between *Shewanella oneidensis* MR-1 and ferrihydrite-phosphate complex from 0.81 ± 0.064 fJ to 1.92 ± 0.049 fJ, accelerating microbe-mineral bonding up to 5-fold and boosting electron utilization efficiency from 0.015−0.028 h^{-1} to 0.048−0.12 h^{-1} across diverse Fe(III) minerals. We further reveal riboflavin binding hotspots on outer membrane *c*-Cyts, with a binding free energy of −25.6 kJ mol^{-1}. These thermodynamic findings facilitate EET, which in turn significantly enhances the bioavailability of iron and phosphorus. For the first time, we quantified microbial cell-mineral and ES-cell binding energetics, thereby bridging interfacial thermodynamics across molecular and cellular scales to establish a mechanistic basis for EET and its role in nutrient mobilization. Such insights open avenues for control of ES-mediated functions in nutrient cycling, pollutant transformation, and sustainable bioenergy.

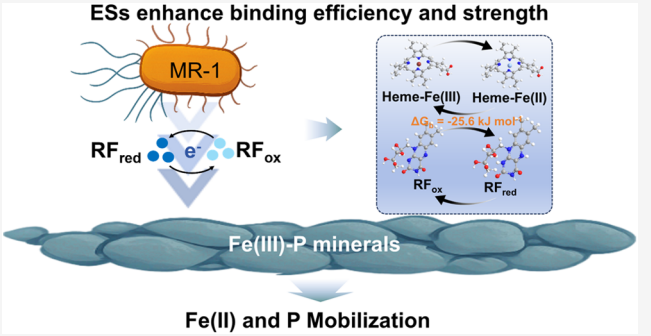

KEYWORDS: *AFM-based force spectroscopy, extracellular electron transfer, electron shuttles, mineral-microbe interface, binding energies*

INTRODUCTION

Extracellular electron transfer (EET) is a fundamental process occurring in superficial and subsurface environments in the Earth, driving microbial metabolism and evolution and the biogeochemical cycling of multiple elements.[1−3] Particularly in waterlogged habitats, EET-driven iron (Fe) redox cycling acts as a core biogeochemical engine, influencing the fate of contaminants and driving the mobilization of phosphorus (P) through Fe−P coupling.[4−9] The resulting release of bioavailable Fe(II) and phosphate is of fundamental importance, as it directly regulates nutrient availability for plants and shapes the metabolism of surrounding microbial communities, thereby determining key ecological outcomes such as primary productivity and ecosystem functioning. However, the efficiency of EET is constrained by multiple factors, including redox potential fluctuations, microbial activity, and mineral properties.[7,10−12] Electron shuttles (ESs), such as natural organic matter, quinones, and flavins, play a crucial role in overcoming these limitations by mediating long-range EET between microbes and Fe(III) minerals.[13,14] Thus, ESs' role in mediating efficient electron transfer is key to optimizing microbial-mineral interactions, thereby promoting the release of essential nutrients such as Fe(II) and P in waterlogged systems.

Electron shuttles (ESs) function as mobile redox mediators that accept electrons from microbial cytochromes, then diffuse to reduce Fe(III) minerals. They often associate closely with membrane-bound reductases and form an electron buffer that enhances EET efficiency.[13] Studies in model microorganisms such as *Shewanella oneidensis* MR-1 have clarified key electron transfer pathways, including those involving outer-membrane cytochromes and inner-membrane oxidases, and have shown that ESs increase bioelectrochemical current densities while

Received: December 5, 2025
Revised: April 24, 2026
Accepted: April 24, 2026
Published: May 2, 2026

reducing interfacial charge-transfer resistance. However, the efficiency of ES-mediated EET is governed by the thermodynamic properties of both the ESs and the interface. Although certain parameters such as redox potentials are well understood,[15,16] other critical thermodynamic parameters, such as mineral-microbe binding energies during electron transfer between ESs and outer-membrane *c*-Cyts,[17] are still poorly understood (Figure 1A). Therefore, understanding the thermodynamic mechanisms behind ES-enhanced EET, especially at mineral-microbe interfaces, remains a challenge when using conventional methods.

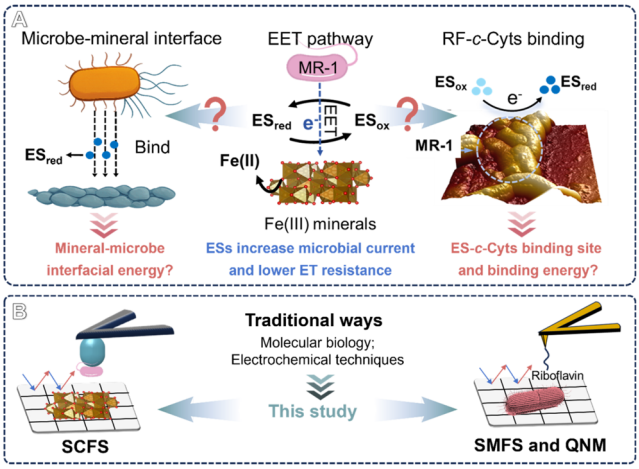

Figure 1. Elucidating ES-mediated microbial EET: from established pathways to unquantified interfacial thermodynamics. (A) Traditional ways, such as molecular biology and electrochemical techniques, have demonstrated the EET pathway of *S. oneidensis* MR-1 and the role of ESs in microbial electrochemical parameters, while key thermodynamic parameters, such as binding strength at mineral-microbe interfaces and binding energy of electron transfer between cytochromes and ESs, remain unquantified. (B) The multidimensional approach combining AFM-based force spectroscopy with QNM to investigate EET at the mineral-microbe interface in this study. Abbreviations: ES, electron shuttle; ES_{red}, reduced electron shuttle; ES_{ox}, oxidized electron shuttle; EET, extracellular electron transfer; *c*-Cyts, c-type cytochromes; RF, riboflavin; SCFS, single cell force spectroscopy; SMFS: single molecular force spectroscopy; QNM, quantitative nanomechanical mapping.

Molecular and physiological techniques, though useful for establishing causal relationships in EET pathways, are often time-consuming and cannot directly measure thermodynamic parameters.[18−20] Electrochemical methods efficiently evaluate kinetics and electron flux, but struggle to fully capture complex thermodynamic processes, such as quantifying the thermodynamic contribution of ESs in mediating EET at the mineral-microbe interface.[20−22] While theoretical calculations can predict reaction energies,[23−25] they tend to oversimplify microbial surface processes and cannot consider the complexed reaction conditions. Consequently, a fundamental limitation remains, as traditional methods lack the ability to directly measure the thermodynamic parameters that arise when an ES-mediated mineral-microbe contact, particularly in a high spatial and temporal resolution. Atomic force microscopy (AFM) has become a novel tool for probing interfacial processes in microbiology. Force spectroscopy measures interaction forces and extracts binding strength, including adhesion force, adhesion energy, and binding energy in real time. Meanwhile, quantitative nanomechanical mapping (QNM) visualizes nanoscale adhesion hotspots (Figure 1B). Their integration builds a thermodynamic framework that connects molecular interactions to EET kinetics and correlates parameters with outcomes such as Fe(II) production and the consequent release of phosphate.

To bridge this knowledge gap, we developed an innovative approach that combines AFM-based force spectroscopy with QNM, enabling direct quantification of thermodynamic parameters governing EET at the mineral-microbe interface. Here, we selected a model electroactive microbe, *S. oneidensis* MR-1, riboflavin (RF) as the ES, and various Fe(III) minerals (ferrihydrite, goethite, amorphous Fe(III)-phosphate, and strengite) as electron acceptors. We applied single-cell force spectroscopy (SCFS) to directly quantify mineral-microbe binding strength and to reveal the thermodynamic mechanism by which RF enhances EET efficiency at the mineral-microbe interfaces. Next, we investigated the relationship between mineral-microbe interfacial binding, including adhesion forces and adhesion energies, and Fe(II) generation kinetics. Then, we utilized AFM-QNM to visualize the specific binding of ESs to EET-functional proteins and conducted single-molecular force spectroscopy (SMFS) to quantify the binding energy required for ET. Finally, we assessed the environmental P release effects resulting from the promotion of EET by ESs. This work uniquely bridges the knowledge gap by directly probing the thermodynamic mechanisms of ES-enhanced EET at relevant biological-mineral interfaces and quantifying ES contributions to electron flux, transfer efficiency, and binding energetics, ultimately linking these molecular-scale energetics to the acceleration of Fe cycling and P mobilization. This provides a new methodological foundation for studying ES-mediated EET processes and their critical role in regulating coupled Fe−P dynamics and nutrient supply across environmental and agricultural contexts.

MATERIALS AND METHODS

Materials and Cell Culture

A list of all chemicals used is provided in Supporting Information, Text S1. The wild type (WT) stain of *S. oneidensis* MR-1 was purchased from China Center of Industrial Culture Collection. *S. oneidensis* MR-1 was aerobically cultured in LB medium (5 g L^{-1} NaCl, 5 g L^{-1} yeast extract, 10 g L^{-1} tryptone) at 200 rpm for 12 h at 30 °C. To ensure experimental consistency, *S. oneidensis* MR-1 cells in all experiments were aerobically grown to the midexponential phase in a LB medium at 30 °C (Figure S1). The suspension was then centrifuged at 5000 rpm for 8 min at 5 °C, washed three times with sterilized PIPES buffer (Sigma-Aldrich), and resuspended in PIPES buffer to the required OD value for the experiment. The pH of the microbial suspension was adjusted to 7.0 using 30 mM PIPES.

Single-Cell Force Spectroscopy (SCFS)

To quantify the thermodynamic profile of EET at mineral-microbe interfaces, single-cell force spectroscopy (SCFS) experiments were conducted to measure the adhesion force and adhesion energy at different contact times (0.3, 1, 5, and 10 s). *S. oneidensis* MR-1 cells were modified onto AFM Si_3N_4 probes with a 5 μm radius (MLCT-SPH-5UM, Bruker) using a dopamine solution.[26] Detailed procedures for AFM probes functionalization with *S. oneidensis* MR-1 cells are described in the Supporting Information, Text S2. Adhesion force/energy was not normalized by contact area because a single intact cell of similar size was attached to a spherical probe, and all RF comparisons were performed under identical loading/contact conditions with the same probe and mineral, making relative trends robust to small area variations. Given that locally secreted RF can

https://doi.org/10.1021/acs.est.5c17543
Environ. Sci. Technol. 2026, 60, 13414−13426

reach micromolar levels in microenvironments such as cell surfaces or biofilms,[27,28] we thus selected RF/AQDS concentrations of 0, 20, and 40 μM for subsequent experiments. PIPES buffer, containing 10 mM sodium lactate and 0, 20, or 40 μM RF/AQDS, was purged with 99.99% N_2 for 1 h under sterile conditions. The solution was then introduced into the AFM liquid cell at a constant flow rate of 2 mL h^{-1} using four types of Fe(III) minerals bound with phosphate as extracellular electron receptors. The detailed synthesis and characterization of Fe(III) minerals bound with phosphate can be found in Supporting Information, Text S3 and Figures S2−S3. The Force Volume mode was used, with the tip manually engaged. Adhesion energies between *S. oneidensis* MR-1 and Fh-P complex were measured at retraction velocities of 200, 1040, 1900, and 3910 nm s^{-1} with 0 and 40 μM RF/AQDS. Retraction rates ≤ 200 nm s^{-1} were confirmed to lie within a near-equilibrium region (Figure S4), in agreement with previous studies.[23,29] Accordingly, a retraction velocity of 20 nm s^{-1} was employed for equilibrium interfacial measurements to minimize dynamic dissipation and better capture the thermodynamic nature of adhesion. Parameters were set as follows: a forward approach velocity of 200 nm s^{-1} and a retraction velocity of 20 nm s^{-1}. Retraction delays of 0.3, 1, 5, and 10 s were applied, with a trigger threshold of 0.5 V. The spring constant of the probe was calibrated prior to all experiments. Force−distance curves were collected at 256 positions on a 1 × 1 μm^2 area of each of the four Fe(III) minerals. All cells used for force spectroscopy experiments were harvested at the exponential growth phase. The analysis comprised a minimum of 200 force−distance curves per experimental condition, acquired using at least three independent single-cell-functionalized probes per mineral substrate.

Quantitative Nanomechanical Mapping (QNM) and Single-Molecule Force Spectroscopy (SMSF)

For QNM experiments, 12-mercaptododecanoic acid was used as a cross-linking agent to functionalize RF onto gold-plated AFM probes. Detailed RF-functionalized AFM probes can be found in Supporting Information, Text S4. *S. oneidensis* MR-1 were suspended in a PIPES buffer containing 10 mM sodium lactate, 10 mM $FeCl_3$ with the OD_{600} value adjusted to 0.2 and the pH set to 7.0. Three treatments were set: 1. *S. oneidensis* MR-1 suspensions before ultrasonic treatment purged with 99.99% N_2 for 0.5 h in a sterile operating console; 2. *S. oneidensis* MR-1 suspensions after ultrasonic treatment purged with 99.99% N_2 for 0.5 h in a sterile operating console. 3. *S. oneidensis* MR-1 before ultrasonic treatment and exposed to air. Subsequently, a freshly cleaved mica (001) surface was used as the substrate, and *S. oneidensis* MR-1 suspensions under different treatments were introduced into the AFM liquid cell at a constant flow rate of 2 mL h^{-1} until *S. oneidensis* MR-1 deposited onto the mica (001) surface. QNM mode was employed, with the probe manually engaged and the spring constant of probe calibrated. The spatial resolution of hotspot features is defined by the QNM pixel size (2 nm per pixel for a 6 × 6 μm^2 map with 512 × 512 pixels) and the effective tip−sample contact radius (~2 nm). High-binding hotspots were reproducible across repeated scans at the same location under identical imaging conditions, with consistent hotspot position and intensity. Scanning was conducted at a rate of 1 Hz over a 10 × 10 μm^2 area, simultaneously capturing height and morphology images of *S. oneidensis* MR-1, as well as an adhesion force map between RF and a *S. oneidensis* MR-1 surface.

To further quantify the binding energy (ΔG) in the electron transfer process between *c*-Cyts and RF, SMFS experiments were conducted. These experiments were carried out in a fluid cell to examine the binding force between an RF-functionalized tip and the outer membrane *c*-Cyts under anaerobic conditions. To ensure that RF could undergo EF with *c*-Cyts during the tip approach-retraction cycle, the solution needs to contain 10 mM sodium lactate and 10 mM $FeCl_3$, buffered at pH 7.0 with PIPES. The force volume mode was employed after calibrating the probe's radius, sensitivity, and elastic coefficient. Force−distance curves were obtained from RF-modified tips and *S. oneidensis* MR-1 outer membranes at 256 distinct positions across a 2 × 2 μm^2 area. These measurements were taken at a forward velocity of 200 nm s^{-1} and variable retraction velocities of 20, 200, 1040, 1900, and 3910 nm s^{-1}. The ΔG between RF and *c*-Cyts was then calculated using the Friddle-Noy-DeYoreo model.[29] Detailed calculations are provided in the Supporting Information, Text S5. To avoid microbial EPS-induced probe contamination, we monitored the separation distance in force−distance curves in real time during SMFS measurements; this distance increases significantly upon contamination owing to the polymeric nature of EPS. Both QNM and SMFS measurements were performed in triplicate with independent biological replicates.

Dissolution Kinetics Experiments

The batch microbial reduction experiments were carried out in 50 mL sterile serum bottles under anaerobic conditions for 6 days. *S. oneidensis* MR-1 suspensions were added to the final OD_{600} of 0.8. Sodium lactate was then added as an electron donor to a final concentration of 10 mM. To maintain anaerobic conditions, the microbial suspension containing sodium lactate was purged with 99.99% N_2 for at least 1 h in a sterile operating console to ensure complete removal of O_2 from the culture environment. Next, Fe(III) minerals bound with phosphate were added as extracellular electron acceptors, with a final concentration of 1 g L^{-1}. The experiments were conducted under different RF/AQDS concentrations (0, 20, and 40 μM) to study the effect of RF/AQDS on EET and phosphate release. The serum bottles were shaken in a 220 rpm at 30 °C. Dissolved P and total Fe(II) were measured at each sample point. All experiments were repeated at least three times. The concentration of aqueous phosphate was analyzed by molybdenum blue colorimetric method using a UV−vis spectrophotometer (Persee, China) at 700 nm. For total Fe(II) measurement, 1.0 mL of unfiltered suspension was added to 4 mL of deoxygenated 1.25 M HCl (final concentration ~ 1 M HCl), extracted with shaking for 1 h at room temperature, and analyzed by the o-phenanthroline method at 510 nm.[30] This 1 M HCl extraction dissolves amorphous iron oxides, adsorbed Fe(II), and secondary iron minerals (e.g., magnetite, green rust). The pH and conductivity were monitored throughout incubations.

In the *in situ* AFM dissolution experiments, a Gt-P complex was selected as the substrate because of its unique shape, which facilitates the *in situ* observation of its dissolution dynamics at the microscopic scale. The microbial suspensions (pH 7.0, OD_{600} = 0.8, 10 mM sodium lactate, and 0 or 40 μM RF) purged with 99.99% N_2 for at least 30 min, then shaken in a 220 rpm at 30 °C for 1 d. Prior to introducing the suspension, N_2-purged ultrapure water was first introduced into the AFM liquid cell to ensure a low-oxygen environment. Afterward, microbial suspensions were filtered through a 0.22-μm membrane filter into the AFM liquid cell at a constant rate of 2 mL h^{-1}. AFM images were acquired with ScanAsyst-Fluid+ tips in ScanAsyst mode, using a scan rate of 2.0 Hz at 25 °C and a scan range of 1.5 × 1.5 μm^2. The images obtained were analyzed using NanoScope software.

Spectroscopy and Electrochemistry Experiments

The concentration of RF_{ox} was determined spectrophotometrically at 375 nm using a UV/vis spectrophotometer according to the calibration curves (Figure S4A). The absorbance kinetics of RF were measured with a wavelength range of 220−400 nm and a scan speed of 1.0 nm/s. Following the methods of Luo et al.,[31] a horse heart cytochrome *c* was used as a standard to measure the concentration of reduced *c*-Cyts in intact cells via diffuse transmittance UV/Visible (DT-UV/vis) spectrophotometry at 552 nm according to the calibration curves (Figure S4B). The absorbance kinetics of *c*-Cyts were analyzed in the wavelength range of 300−600 nm with a scan speed of 1.0 nm s^{-1}. Details of RF and *c*-Cyts determinations can be found in the Supporting Information, Text S6. To further investigate the redox state of RF at the molecular scale, Raman spectroscopy was conducted with spectra collected in the 1000−1800 cm^{-1} range using a 532 nm laser. Additionally, Raman spectroscopy was employed to characterize the redox state of *c*-Cyts in living cells, with spectra acquired in the 1200−1700 cm^{-1} range using a 785 nm laser that was operated at low power (≤1 mW at the

https://doi.org/10.1021/acs.est.5c17543
Environ. Sci. Technol. 2026, 60, 13414−13426

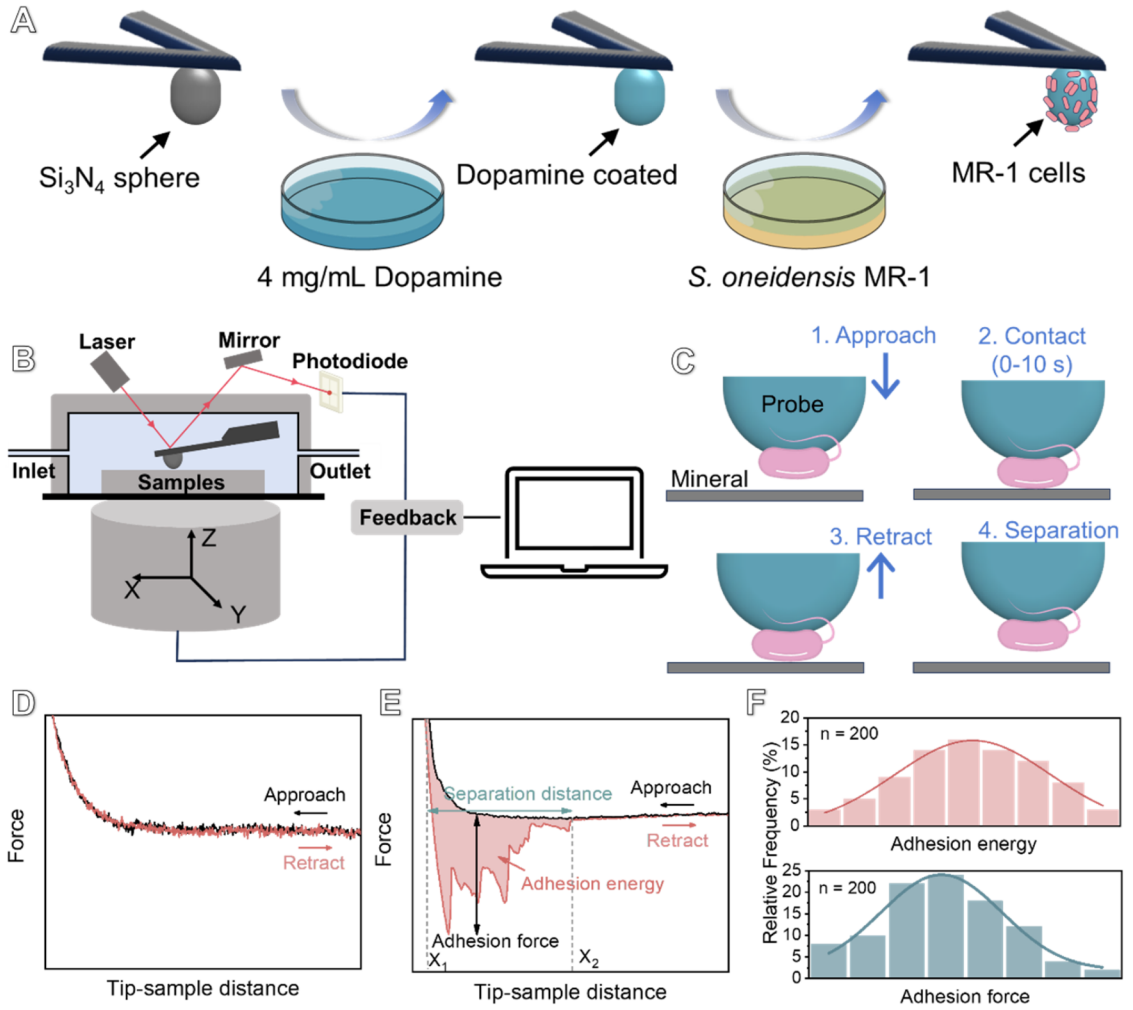

Figure 2. AFM-based force spectroscopy setup and analysis. (A) Schematic of the AFM probe functionalization with *S. oneidensis* MR-1. (B) In the fluid cell, a laser focuses on the cantilever backside, and reflected light is detected by a photodiode to measure deflection. Tip−sample interfacial forces in liquid are converted to force data in real-time, triggering a piezo feedback system to adjust the sample position. (C) In SCFS, the probe undergoes an approach-contact-retract cycle with the substrate surface, generating a force−distance curve. (D) A bare probe and (E) an *S. oneidensis* MR-1 functionalized probe interact with a mineral substrate, generating force−distance curves. (F) Then, adhesion forces and adhesion energies can be extracted from the force−distance curves and analyzed by fitting with a Gaussian distribution.

sample) with a short exposure time of 10 s per acquisition to minimize laser-induced artifacts.

The effect of RF on the electrochemical activity of MR-1 was studied by cyclic voltammetry, electrochemical impedance spectroscopy and differential pulse voltammetry using an electrochemical workstation (CHI660D, China) in a typical three-electrode system with an Ag/AgCl electrode as reference electrode at 30 °C. Detailed electrochemical measurements can be found in Supporting Information, Text S7.

RESULTS AND DISCUSSION

Setting up a SCFS System to Thermodynamically Quantify Mineral-Microbe Interactions

To investigate the role of ESs in regulating mineral-microbe binding strength, we developed an innovative approach using an SCFS system. In this approach, *S. oneidensis* MR-1 cells were functionalized onto a spherical AFM probe with a radius of 5 μm (Figures 2A and S5). Figure 2B illustrates the experimental configuration employing a fluid cell integrated with high-sensitivity, real-time laser-based cantilever deflection detection and nanometer-precision piezo feedback control.[32] This advanced setup enables quantitative force measurements under various liquid conditions. During SCFS, we systematically measured the binding strength between an individual microbial cell and a mineral substrate by performing repeated approach-contact-retract cycles (Figure 2C).

Each cycle generated characteristic force−distance curves, from which two critical parameters, adhesion force and separation distance between the cell and substrate surface were extracted. The bare probe showed no significant adhesion force with a mineral substrate varying RF concentration from 0 to 40 μM (Figures 2D and S6). To exclude artifacts from the dopamine coating used for cell immobilization, we performed control force spectroscopy with dopamine-coated probes on Fh-P; RF did not measurably change the adhesion force or separation distance (Figure S7), indicating that the RF-dependent effects arise from the cell-mineral interface rather than dopamine-mineral interactions. Notably, in the force−distance curve obtained using a single-cell-functionalized probe and a mineral substrate, the area enclosed between the approach and retraction curves quantitatively represents the adhesion energy dissipated during bacterial detachment from the mineral surface (Figure 2E), providing a thermodynamic

https://doi.org/10.1021/acs.est.5c17543
Environ. Sci. Technol. 2026, 60, 13414−13426

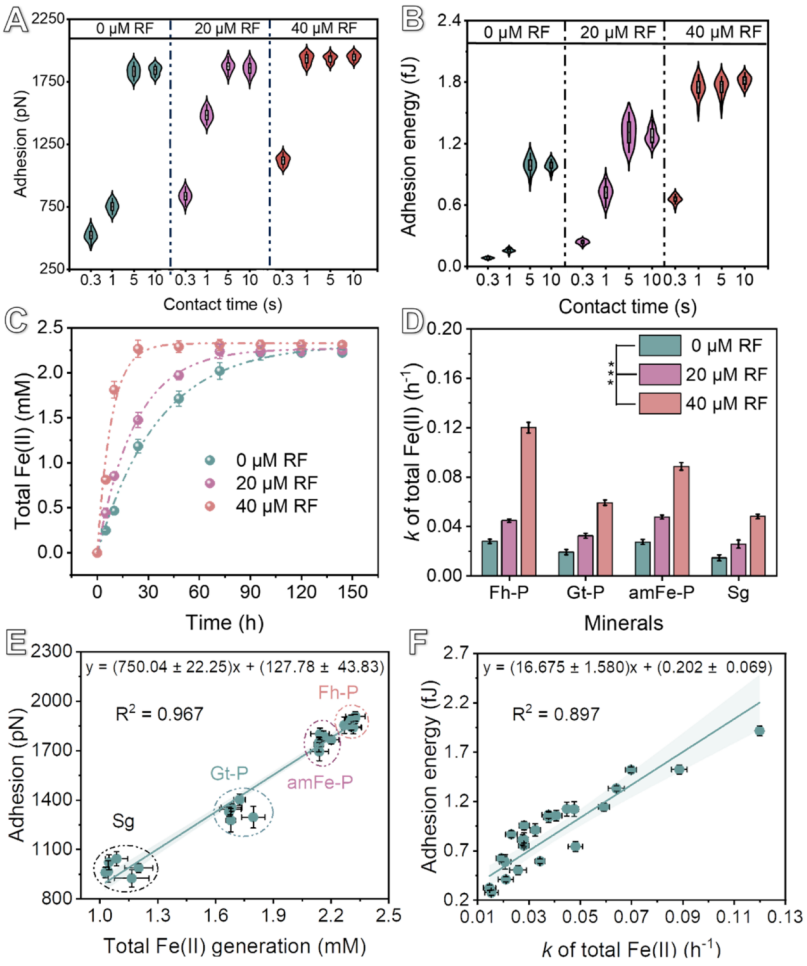

Figure 3. The correlation relationship between mineral-microbe binding strength and EET kinetics. (A) Adhesion forces and (B) adhesion energies measured between *S. oneidensis* MR-1 and Fh-P complex under 0, 20, and 40 μM RF concentrations, with contact times of 0.3, 1, 5, and 10 s, in a 10 mM sodium lactate, pH 7.0 (PIPES buffer) solution, and an N_2 exposure for 20 min. In solutions with pH 7.0, OD600 = 0.8, 10 mM sodium lactate, varying RF concentrations, and 1 g L^{-1} Fh-P complex (C) the kinetics of Fe(II) production and (D) the rate constant *k*, fitting by pseudo-first-order, were analyzed during extracellular respiration of *S. oneidensis* MR-1. (E) Correlation between adhesion force and total Fe(II) generation, illustrating the relationship between mineral-microbe binding and EET flux. (F) Correlation between adhesion energy and the rate constant (*k*) of Fe(II) generation, highlighting the role of adhesion energy in regulating EET efficiency at the mineral-microbe interface.

measurement of bond stability.[33] Given the stochastic nature of mineral-microbe interactions, the binding strength between microbes and minerals naturally follows a probability distribution.[34] To ensure the reliability and representativeness of the results, each condition was replicated with at least three biologically independent cultures, and multiple technical measurements were performed across distinct surface sites on each cell. The frequency histograms of adhesion forces and adhesion energies, derived from these force curves, were then analyzed and fitted using a Gaussian distribution to capture the central tendency and variability of the binding interactions (Figure 2F). Our high-throughput AFM technique overcomes conventional limitations by integrating nanoscale force resolution with the ability to directly quantify the thermodynamic forces that drive microbial EET in real time, thus revealing the fundamental mechanisms by which ESs promote microbial EET efficiency.

The Binding Strength at Mineral-Microbe Interfaces with Varying Riboflavin Concentrations

To determine the role of RF in mineral-microbe binding strength, we obtained and analyzed the force−distance curves under different contact times via SCFS. The stable and tight mineral-microbe connections formed under different contact times directly support microbial EET, and the changing process of the binding strength during their establishment appropriately reflects the kinetic characteristics of the EET interface formation. Our measurements revealed that at RF concentrations of 0, 20, and 40 μM, the adhesion forces measured during the retraction of *S. oneidensis* MR-1-functionalized probes from Fh substrates after a 10-s contact were approximately 1850 pN, with no significant difference observed across the different concentrations (Figure S8). This indicates a strong and specific interaction between the microbial cell and the Fh surface.[35] Notably, while RF concentration did not affect the maximum adhesion force between *S. oneidensis* MR-1 and the same Fe(III) mineral, it significantly reduced the contact time needed to reach this force (Figure 3A). Specifically, increasing RF concentration from 0 to 40 μM enhanced the adhesion efficiency 5-fold, from 370 pN s^{-1} to 1890 pN s^{-1}, demonstrating significantly accelerated binding kinetics. Higher RF concentrations resulted in faster adhesion force kinetics (Figure S9), leading to higher electron transfer rates by reducing the time required for microbial cells to establish contact and initiate EET.

https://doi.org/10.1021/acs.est.5c17543
Environ. Sci. Technol. 2026, 60, 13414−13426

Additionally, shorter binding kinetics facilitate more frequent redox cycles per unit time, thereby increasing electron throughput to minerals and further promoting microbial EET.[36] Our data revealed that the adhesion force varied depending on the type of mineral substrate, with differences observed across various Fe(III) minerals (Table S1).

The mineral-microbe binding strength was further quantified. In the absence of RF, force−distance curves displayed only a few discrete rupture steps (Figure S8), indicating short-range specific binding between surface *c*-Cyts and mineral sites. Upon adding 20−40 μM RF, the number of rupture steps increased, and the effective separation distance was significantly extended from 582 to 944 nm, demonstrating that RF dominates the interfacial interaction between *S. oneidensis* MR-1 and Fh-P. These changes reveal that RF binds strongly to microbial *c*-Cyts and thermodynamically stabilizes the microbe-mineral interface, directly contributing to the thermodynamic driving force for interfacial electron transfer. As the RF concentration increased from 0 to 40 μM, the separation distance between the microbial cells and the substrates increased from 580 to 944 nm, resulting in a 1.8 to 2.4-fold increase in adhesion energies (Figure 3B and Tables S2−S3). In addition to RF, we introduced AQDS as a well-known ES and performed parallel SCFS measurements under the same conditions. AQDS produced the same qualitative trends as RF, increasing adhesion force kinetics and adhesion energies, promoting faster establishment of interfacial binding (Figure S10 and Tables S4−S6). This indicates that the strengthening of mineral-microbe binding is not unique to riboflavin but is a general feature of redox-active shuttles. This increase in adhesion energy with RF concentration suggests that RF stabilizes the mineral-microbe interaction, making the binding more persistent. While organic molecules may intuitively seem less likely to strengthen such an interface mechanistically, we propose that RF acts as a bridging ligand or interfacial mediator. The isoalloxazine ring of RF is capable of forming specific, multivalent interactions with both the mineral surface through hydrogen bonding, electrostatic interactions, or coordination with surface metals.[11,37,38] Additionally, it interacts with biomolecules such as proteins and glycans on the microbial cell surface.[13] This simultaneous binding effectively "glues" the microbe to the mineral, increasing the effective contact area and the number of binding sites, thereby enhancing both adhesion energy and stability. This bridging function aligns with RF's known role as an electron shuttle bound at interfaces during microbial EET. Such enhanced stability is crucial for long-term microbial-mineral interactions in dynamic natural environments, where stable contact between cells and solid-phase electron acceptors ensures sustained EET.

Furthermore, we investigated the relationship between mineral-microbe binding strength and microbial EET. Although electron-donor availability influences overall flux, we fixed lactate concentration to isolate interfacial binding effects (Figure S11). Observed trends therefore primarily reflect shuttle-mediated interfacial kinetics, not donor-dependent regulation. The kinetics of total Fe(II) generation were determined during extracellular respiration by *S. oneidensis* MR-1. Batch experiment results showed that increasing the RF concentration significantly accelerated Fe(II) generation rates by 3.1 to 4.3 times (Figures 3C−D and S12), suggesting that RF enhanced EET efficiency and accelerated the reductive dissolution process. This implies that adhesion energy is important in microbial-mineral interactions, where stronger and more persistent binding translates to more efficient EET. Additionally, the total Fe(II) production and the k values followed the order: Fh-*P* > amFe-*P* > Gt-*P* > Sg. This trend reveals that mineral properties, including crystallinity, specific surface area, and surface charge collectively govern microbial EET flux and efficiency.[34] Consistent with this, Fh exhibited the highest reactivity, which we attribute to its large surface area and more positive surface charge under the experimental conditions (Figure S13). However, the Zeta potential data indicated that although phosphate adsorption significantly reduced the surface potential of Fh and Gt, the extent of RF-mediated EET enhancement was not proportional to these electrostatic changes. Specifically, although the negative shift amplitude of the Zeta potential of Fh-P was greater than that of Gt-P (Figure S14), the increase in RF-mediated EET efficiency and adhesion energy in the Fh-P system was only 1.37−2.03 times and 1.23−1.67 times that of the Gt-P system, respectively (Figure 3D, Table S3 and S6). This discrepancy was inconsistent with the simple electrostatic shielding mechanism of RF. Increasing RF raised Fe(II) rates but not equilibrium extent, and AQDS produced the same qualitative effect (Figure S15). These results show that, across minerals with different surface properties, higher adhesion forces at the mineral-microbe interface were linked to greater Fe(II) generation. Conversely, for a given mineral substrate, increasing RF concentration boosted adhesion energy, speeding up the rate of Fe(II) generation.

To further verify this, we examined the correlation between the binding strength at mineral-microbe interfaces and Fe(II) generation kinetics under both RF and AQDS treatments, uncovering the implications of mineral-microbe binding for EET flux and efficiency. A positive correlation was observed between the total Fe(II) production amount and adhesion force at the mineral-microbe interfaces (R^2 = 0.967), and between total Fe(II) production rate and adhesion energy (R^2 = 0.897) (Figure 3E-F). Since the production of Fe(II) is mediated by *S. oneidensis* MR-1, the total amount of Fe(II) produced in the system can serve as a direct quantitative indicator to evaluate the mineral reductive capacity and microbial EET flux under various experimental treatments. The pseudo-first-order rate constant (k) quantitatively reflected microbial EET efficiency. To distinguish interfacial energetic coupling from coincidental adhesion enhancement, we compared redox active mineral systems with inert substrates. RF increased binding kinetics and adhesion energy on Fe(III) minerals but produced no enhancement on mica (Figure S16), indicating that the adhesion increase is not a generic physicochemical adsorption effect. Moreover, stronger binding strength signatures including higher adhesion energy, more rupture steps, and longer interaction distances consistently showed faster Fe(III) reduction. This cross scale correspondence argues against incidental adhesion and supports a mechanistically relevant interfacial coupling. These results suggested that, as thermodynamic indicators of interfacial bonding strength, adhesion force and adhesion energy reflect microbial EET flux and efficiency at the mineral-microbe interface, respectively. This implies that microbial-mineral contact, particularly in biogeochemical processes, is an active and energy-dependent process that can be modulated by ESs like RF.[13,39] Although shuttle-mediated EET can, in principle, become limited by mediator diffusion, Fe(II) accumulation/removal, or saturation at high RF, these

https://doi.org/10.1021/acs.est.5c17543
Environ. Sci. Technol. 2026, 60, 13414−13426

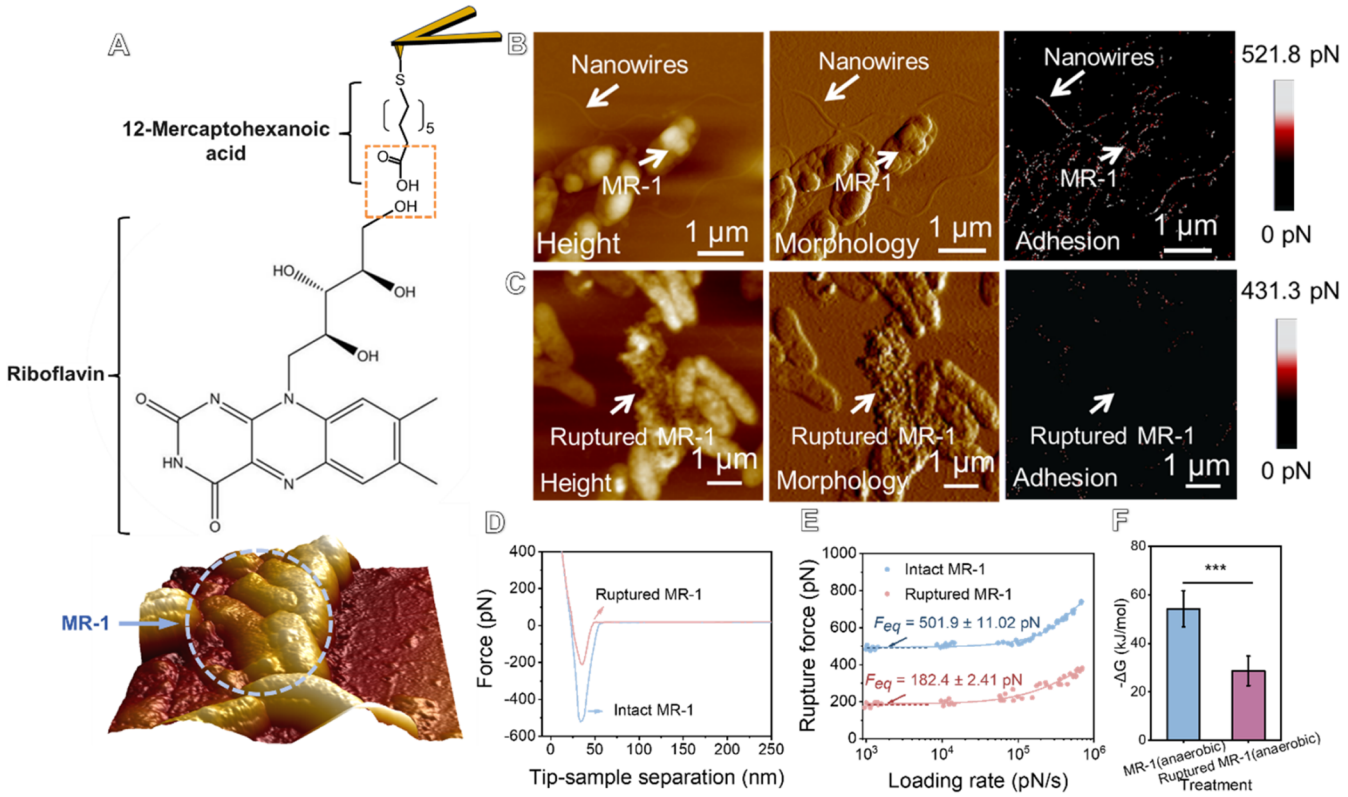

Figure 4. Visualization and thermodynamic quantification of electron transfer between RF and outer membrane *c*-Cyts. (A) Schematic diagram of an AFM probe functionalization with RF, which was subsequently used for AFM-QNM experiments. AFM height, morphology image, and rupture force mapping between RF and *S. oneidensis* MR-1 outer membrane (B) before and (C) after ultrasonic treatment. (D) Representative force−distance curves of RF interacting with *S. oneidensis* MR-1 under different treatments. (E) Binding force vs loading rate showing an increasing rupture force with increasing loading rate. The equilibrium binding force was fitted using the Friddle-Noy-DeYoreo model. Then, (F) the binding energies of RF-modified tips and *S. oneidensis* MR-1 outer membrane under different treatments were calculated.

transport-controlled effects were intentionally not probed in the present study. Our experimental design fixed mixing conditions, cell density, and mineral loading to minimize variability from mass-transfer processes, thereby enabling a focused assessment of how interfacial adhesion energetics (measured by SCFS) relate to EET kinetics across mineral types and RF concentrations. Under these controlled conditions, the strong correlation between adhesion energy and Fe(II) production rate supports an interfacial-energetic control on kinetics. Specifically, the enhanced microbe-mineral binding mediated by RF create a more favorable micro-environment for faster ET through three key mechanisms: (1) shortening the physical distance between *c*-Cyts and Fe(III) sites (or adsorbed RF), thereby reducing the activation energy for interfacial electron tunneling; (2) stabilizing the relative positions at the interface over longer time scales, increasing the probability and duration of efficient electronic coupling; and (3) minimizing interfacial water layers or gaps, effectively constructing a more robust physical conduit. Consequently, high adhesion force increased the density of stable contact points at the mineral-microbe interface, promoting greater Fe(II) production. Meanwhile, the high adhesion energy effective coupling and maintained the optimized ET pathway, accelerating Fe(II) production rate. Cyclic voltammetry (CV), differential pulse voltammetry (DPV), and electrochemical impedance spectroscopy (EIS) further supported these findings (Figure S17). CV and DPV revealed that the redox peaks of RF and *c*-Cyts gradually intensified with increasing RF concentration, accompanied by a minor potential shift, indicating enhanced redox activity and interaction. EIS Nyquist plots showed a smaller semicircle diameter and lower fitted charge-transfer resistance at higher RF concentrations, consistent with accelerated interfacial electron transfer. These electrochemical results collectively confirm the RF-mediated interaction with *c*-Cyts.

Abbreviations: Fh-P, ferrihydrite-phosphate complex; Gt-P, goethite-phosphate complex; amFe-P, amorphous Fe(III) phosphate; Sg, strengite.

Visualization and Quantification of Specific RF-*c*-Cyts Binding at Microbe Interfaces

While RF enhances the contact efficiencies and adhesion energies between microbes and Fe(III) mineral surfaces, thereby promoting microbial EET, the fundamental electron transfer mechanism relies on *c*-Cyts-driven transmembrane electron transfer.[40−43] To better understand this process, we further identified the binding sites where ESs dock with membrane-bound *c*-Cyts to harvest electrons, and quantified the binding energy required for electron transfer from *c*-Cyts to ESs across the microbe interface. We functionalized the AFM probe by covalently conjugating RF to a tip through 12-mercaptohexanoic acid cross-linking (Figure 4A). We compared the force curves of the probe before and after functionalization on inert substrates such as mica to validate the functionalization outcome. The results showed that the interaction force between a bare probe and the mica surface was negligible, whereas the RF-functionalized probe exhibited

https://doi.org/10.1021/acs.est.5c17543
Environ. Sci. Technol. 2026, 60, 13414−13426

an interaction force of approximately 130 pN with mica (Figure S18). This relatively weak force was attributed primarily to hydrogen bonding between the RF molecule and the mica surface, confirming that RF-functionalized probe can be specifically used for subsequent quantitative measurements of intermolecular interactions. For *S. oneidensis* MR-1 before ultrasonic treatment, AFM height and morphology images revealed a smooth, intact outer membrane structure, indicative of undamaged and functional cell membranes (Figure 4B). In contrast, *S. oneidensis* MR-1 after ultrasonic treatment exhibited significant membrane disruption, with ruptured and irregular outer membrane structures, increased surface roughness, and decreased elastic modulus (Figures 4C and S19−S20).

Force mapping with RF-functionalized probes revealed spatially heterogeneous, high-adhesion hotspots across the intact outer membrane of *S. oneidensis* MR-1, contrasting sharply with the negligible adhesion observed using bare probes (Figures 4B−D and S21). The nanoscale spatial mapping revealed high-adhesion hotspots on the microbial surface, suggesting specific areas where RF interacts with *c*-Cyts to facilitate microbial EET.[32] In contrast, *S. oneidensis* MR-1 after ultrasonication exhibited a marked decrease in high-adhesion regions (Figure 4C−D), indicating a nonspecific binding, such as RF-phospholipid hydrophobic interactions.[37] Ultrasonication induced *S. oneidensis* MR-1 disruption, ranging from surface structural damage to complete rupture,[38] and these structural alterations likely impair the accessibility of functional *c*-Cyts on the outer membrane. The significant decrease in adhesion strength probably reflects the mechanical disruption of the outer membrane caused by ultrasonication, which may result in partial or complete loss of functional *c*-Cyts from the membrane. To validate this, the concentrations of dissolved *c*-Cyts were measured in microbial suspensions before and after ultrasonication. Ultrasonic treatment significantly elevated supernatant c-Cyts$_{red}$ levels (Figure S22). Raman spectra of *S. oneidensis* MR-1 showed characteristic heme Fe(II) peaks at 1363, 1552, and 1605 cm^{-1},[44] which were markedly decreased after ultrasonication (Figure S23). Together, the increased dissolved c-Cyts$_{red}$ and the weakened Raman signatures indicate loss/detachment of membrane embedded c-Cyts$_{red}$ due to membrane disruption, rather than a simple redox state shift. Additionally, in a solution not exposed to N_2, no high-adhesion regions were observed between RF and intact *S. oneidensis* MR-1 (Figure S24).

This observation indicates a level of spatial organization that was previously difficult to resolve, pointing to targeted areas where RF molecules likely enhance electron transfer by concentrating interactions with *c*-Cyts. The high-adhesion hotspots imply that these interactions may not be uniform across the cell surface but are instead localized, which could maximize electron transfer efficiency in specific regions. This nanoscale adhesion landscape provides direct evidence of specific RF binding to *c*-Cyts clusters, which may be attributed to ET between RF and the heme cofactors in outer membrane *c*-Cyts through π-π stacking interactions.[40,45] Our spectrophotometric and Raman spectroscopic results confirmed staggered redox states of RF and *c*-Cyts (Figure S25). The colorimetric assay revealed alternating oxidation−reduction states between RF and *c*-Cyts, consistent with electron shuttling. Raman spectra further showed a gradual reduction of RF, while *c*-Cyts remained predominantly reduced. These observations support electron transfer from *c*-Cyts$_{red}$ to RF$_{ox}$, enabling sustained EET. As the functionalized probe approached the microbial surface, the RF was maintained in its oxidized state (RF$_{ox}$) by the presence of soluble Fe(III) in the bulk solution, which rapidly reoxidized any adventitiously reduced RF. This ensured that the initial binding interaction occurred specifically between RF$_{ox}$ and *c*-Cyts on the outer membrane. Upon contact, RF$_{ox}$ accepted two electrons from *c*-Cyts to form RF$_{red}$, and the corresponding unbinding forces were recorded during probe retraction. When the probe retracted into the solution, RF$_{red}$ promptly transferred electrons to surrounding soluble Fe(III), thereby regenerating RF$_{ox}$ and completing the redox cycle. This Fe(III)-mediated reoxidation sustained the ES function of RF throughout repeated force measurements. Notably, we revealed the specific binding sites of RF with the nanowires of *S. oneidensis* MR-1. The nanowires also showed high binding forces to RF (Figure S26), implying that nanowires of *S. oneidensis* MR-1 participate in EET.[46,47] To support their structural identity, our QNM modulus maps showing that the nanowires and cell body exhibit comparable stiffness (≈1.8−1.9 GPa; Figure S27), consistent with outer-membrane extensions rather than type IV pili. The mechanism behind this is related to the structural principle of nanowire formation in *S. oneidensis* MR-1, where nanowires are extensions of the outer membrane that incorporate conductive multiheme *c*-Cyts. Consequently, these wire-like structures exhibit *c*-Cyts-dependent redox activity on their surfaces, enabling specific ES binding and long-range electron transport. More broadly, the strong RF-nanowire interaction suggested that ES can couple not only to membrane proteins but also to extracellular conductive polymers/filaments, potentially enabling more complex three-dimensional EET networks at the community level. Such coupling could facilitate electron relay across neighboring cells and mineral surfaces, enhancing connectivity in biofilms and promoting long-range charge transport.

We further quantified the binding energy (ΔG_b) required for electron transfer between RF and *c*-Cyts. Both equilibrium forces (F_{eq}) and ΔG_b between RF and outer membrane *c*-Cyts decreased significantly after ultrasonic treatments (Figure 4E,F). Since the binding of RF to *S. oneidensis* MR-1 after ultrasonic treatment is a nonspecific interaction, the measured ΔG_b can serve as the baseline value. Accounting for this background, the ΔG_b for two-electron transfer between RF and *c*-Cyts was calculated as approximately −25.6 kJ mol^{-1}. Compared with typical single-electron-transfer processes, this value was averaged to about −12.8 kJ mol^{-1} per electron. This averaging assumes that the two-electron transfer proceeds in a highly concerted manner, as supported by the known redox behavior of the isoalloxazine ring in flavins, where the two reduction steps often exhibit similar potentials.[11,22,40,45] While this simplified division provides a useful thermodynamic estimate for interfacial electron coupling, we note that it does not resolve potential differences between individual electron-transfer steps, which would require more detailed kinetic or potentiometric analysis. Consequently, RF acts as a molecular bridge, facilitating the formation of a highly efficient ternary complex (*c*-Cyts-RF-mineral) that accelerates microbial EET. These findings strongly supported the forward causality that stronger interfacial binding inherently leads to optimized electron tunneling paths and lower interfacial energy barriers, driving faster macroscopic ET rates.

https://doi.org/10.1021/acs.est.5c17543
Environ. Sci. Technol. 2026, 60, 13414−13426

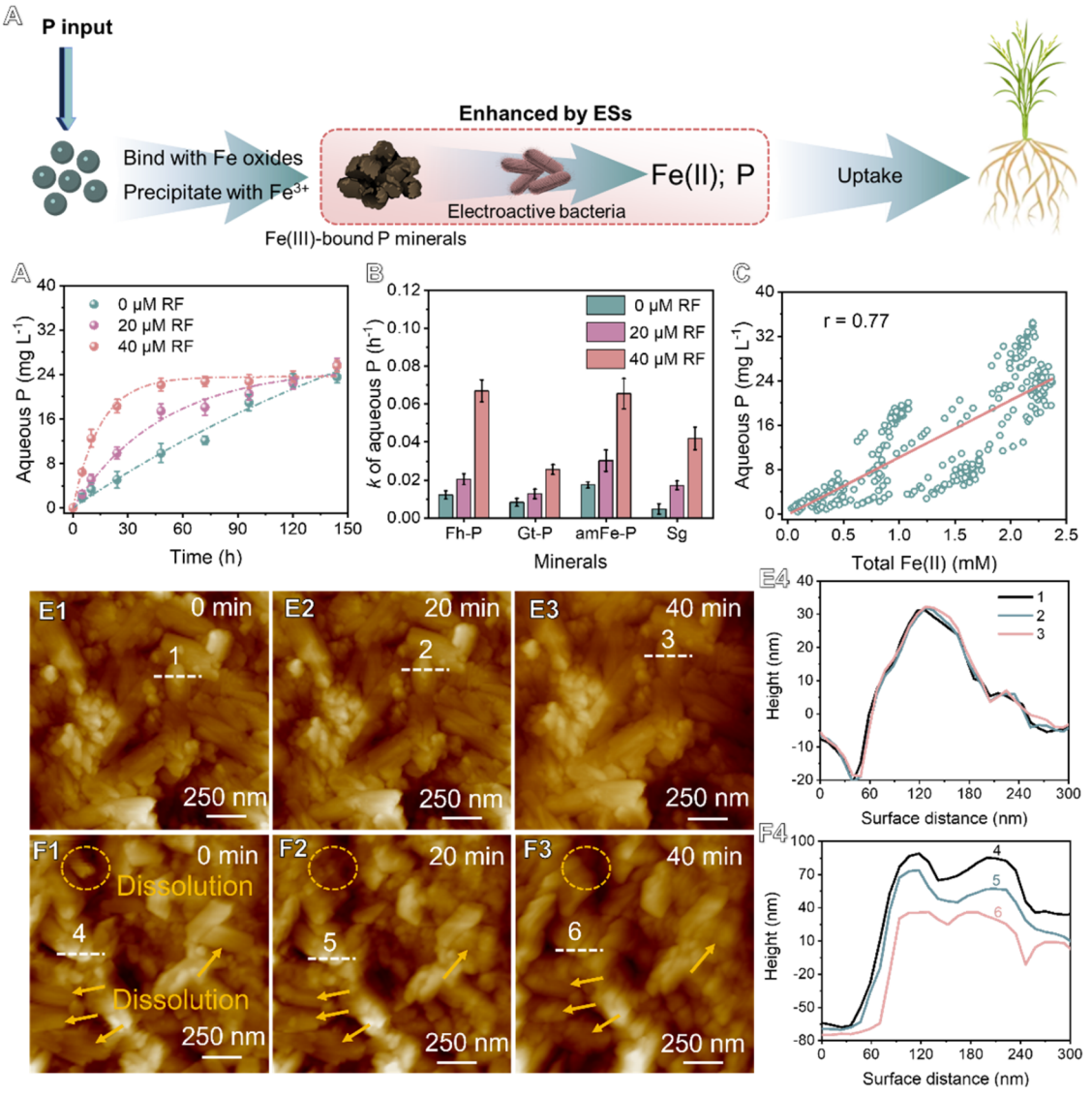

Figure 5. RF enhances Fe(III)-bound phosphate mobilization by *S. oneidensis* MR-1. (A) Simplified schematic of soil extracellular respiration, showing potential pathways for Fe(III)-bound phosphate mobilization. (B) Phosphate release kinetics from Fh-P as an electron acceptor at RF concentrations ranging from 0 to 40 μM. (C) The rate constant k of aqueous P production varies for four Fe(III) minerals (Fh-P complex, Gt-P complex, amFe-P, and Sg), and with changing RF concentrations. (D) Relationship between aqueous phosphate concentration and total Fe(II) concentration during the kinetic reductive dissolution of the four Fe(III) minerals by *S. oneidensis* MR-1 at RF concentrations of 0, 20, and 40 μM. (E, F) Time-sequence AFM height images of the dissolved Gt-P complex (E1-E3) in the absence or (F1−F3) in the presence of RF were obtained. (E4, F4) Height profiles showing the dissolution, measured from (E1-E3) and (F1−F3) along the white dashed lines.

Contributions of ES-Enhanced Fe(III)-Bound Phosphate Release

Through specialized metabolic pathways, electroactive microorganisms mediate the reductive dissolution of insoluble Fe(III) minerals under oxygen-depleted conditions, typically coupled with biogeochemical cycling of associated elements including phosphorus (P).[48] Building on this foundation, our study demonstrates that electroactive microbes, such as *S. oneidensis* MR-1, can effectively mobilize Fe(III)-bound phosphate, with RF enhancing this process by promoting microbial EET (Figure 5A). Since RF concentrations (20 and 40 μM) are orders of magnitude lower than phosphate loadings on Fh and Gt (~350 and ~100 μmol g^{-1}), competitive displacement is negligible. Throughout incubation, pH remained stable (7.00−7.17) due to PIPES buffering, and conductivity differences between RF and RF-free treatments were minimal (Figure S28), indicating that RF did not materially alter bulk ionic content. Accordingly, abiotic RF control experiments released ≤ 2% of sorbed phosphate (Figure S29), confirming that RF alone cannot mobilize P effectively. However, RF significantly enhanced the mobilization of Fe(III)-bound phosphate by *S. oneidensis* MR-1, with kinetic fitting results indicating a 3.2 to 8.5-fold increase in the rate constant (k) as RF concentration increased from 0 to 40 μM (Figures 5B−C and S30). Furthermore. the strong positive correlation between aqueous phosphate concentration and total Fe(II) concentration, with a Pearson correlation coefficient (r = 0.77), confirms that phosphate mobilization is directly coupled to microbial EET (Figure 5D). The increased Fe(II) concentration corresponds to the reduction of Fe(III) minerals, which likely triggers the release of phosphate that was previously bound to these minerals. This coupling of EET and

https://doi.org/10.1021/acs.est.5c17543
Environ. Sci. Technol. 2026, 60, 13414−13426

phosphate release provides a clear pathway for nutrient cycling, particularly in environments where Fe(III) minerals bound with phosphate serve as significant phosphate reservoirs.

At the micronanoscale, AFM results revealed that *S. oneidensis* MR-1 formed nanosized pits on Fe(III) mineral surfaces upon direct contact (Figures S31−S32). However, no dissolution of the minerals is observed when there is no contact (Figures 5E1-E4 and S33), suggesting that microbial-mineral interactions enhance the dissolution of these minerals. Microbes often increase their contact area with minerals, sometimes by producing nanowires, to facilitate Fe(III) reduction and promote mineral dissolution. However, this process is typically limited by the requirement for direct mineral-microbe contact, which constrains the efficiency of reductive dissolution. The introduction of RF enabled *S. oneidensis* MR-1 to reduce and dissolve Fe(III) minerals bound with phosphate even without direct contact (Figures 5F1−F4 and S34−S35), as evidenced by AFM and batch experiments. Notably, a higher-resolution comparative topographic analysis of the two types of dissolution pits, formed by direct contact or RF-mediated contact-free dissolution, revealed that while both are nanoscale, potential morphological differences exist. Pits formed by direct contact often exhibited more localized and steeper-edged features associated with cell attachment points (Figure S31), whereas pits formed under RF mediation tended to be broader, shallower, or showed different spatial distribution patterns (Figures 5F1−F4 and S35). These morphological similarities and differences suggest underlying variations in dissolution kinetics: direct-contact dissolution is likely dominated by reductase enzymes at the tightly attached cell surface, creating a highly localized chemical microenvironment; RF-mediated dissolution, conversely, may proceed via the diffusion and reaction of soluble reductants across the mineral surface, leading to a potentially more diffuse dissolution pattern. These findings suggest that RF, acting as an ES, can effectively enhance EET at a distance, by omitting the need for direct mineral-microbe contact, highlighting the critical role of ESs like RF in optimizing microbial mineral dissolution, particularly in biogeochemical cycles. The ability to mobilize phosphate from mineral surfaces is crucial for nutrient cycling in waterlogged habitats, such as paddy fields and sediments, where Fe(III) and phosphate often coexist. By enhancing microbial EET, RF facilitates the mobilization of Fe(III)-bound phosphate, which can significantly improve nutrient availability in these ecosystems.

Methodological Significance of the Established Platforms

The AFM system provides a spatiotemporal-thermodynamic way to examine mineral-microbe contacts,[49] overcoming the traditional limitation of directly quantifying thermodynamic drivers of EET at live microbial interfaces. The platform provides a capability to synergistically probe adhesion forces, adhesion energies, binding energies, and interaction sites with molecular scale resolution in real time, offering a dynamic view of interfacial processes.[49−52] The technical innovation lies in the platform's ability to map the spatial distribution of ES binding sites while quantifying associated electron transfer energies.[53,54] Through systematic investigations, we demonstrate that the measured thermodynamic parameters serve as robust quantitative predictors of EET flux and efficiency, establishing fundamental relationships between molecular-scale interactions and macroscopic electron transfer phenomena. Real-time monitoring capacity reveals how interaction forces evolve under varying environmental conditions, providing insights into microbial adaptation mechanisms to different electron acceptors. Furthermore, the platform resolves the spatial heterogeneity of ES interactions across cell surfaces, addressing a critical gap in understanding how microorganisms optimize electron transfer strategies at the subcellular level.

Beyond its applications in EET research, this methodology provides a framework for decoding thermodynamic principles governing diverse biogeochemical interfaces. It has the potential to quantify how environmental variables such as pH, ionic strength, and surface properties influence interfacial interactions, facilitating the development of predictive models for microbial behavior in natural environments. By connecting single-molecule events to ecosystem-scale outcomes, the technique shifts microbial electrochemistry toward quantitative prediction. The same methodology can be applied to biofilm formation, pathogen adhesion and syntrophic partnerships, and it may guide the design of more effective bioremediation or medical interventions. When applying SCFS to complex systems such as biofilms, key interpretation challenges include the complexity of force signal origin (e.g., distinguishing cell−substrate, cell−cell, and cell-EPS interactions) and the broad data distributions arising from pronounced heterogeneity. In pathogen adhesion studies, additional challenges involve the dynamic heterogeneity of host surfaces and the multivalent nature of adhesin-receptor interactions, complicating the link between single-bond events and macroscopic phenotypes. For syntrophic partnerships, a core challenge is to design experiments that decouple and quantify the specific, bidirectional physical forces between microbial partners and their interplay with chemical signaling. In short, the AFM platform delivers mechanistic insights into interfacial processes that were previously inaccessible with conventional tools.

■ ENVIRONMENTAL IMPLICATIONS

Within microenvironments like cell surfaces or biofilms, locally secreted riboflavin (RF) can reach micromolar levels, far exceeding typical bulk pore-water concentrations. Thus, it becomes crucial to elucidate the thermodynamic mechanisms by which electron shuttles (ES) like RF mediate extracellular electron transfer (EET) at the microbe-mineral interface. Our work establishes how variations in adhesion energy/force drive changes in ES-boosted EET, which in turn regulates the biogeochemical cycling of phosphorus (P). By precisely measuring how ESs such as riboflavin dramatically accelerate the reductive dissolution of Fe(III) minerals, we reveal a specific microbial mechanism for unlocking mineral-bound P. This process does more than just release phosphate; it also generates bioavailable Fe(II), thereby enhancing the supply of two key nutrients that often limit the growth of both plants and microbes. This understanding points toward new, sustainable approaches to P management. Leveraging this ES-driven mechanism could allow us to selectively release legacy P, which has accumulated over decades of fertilizer or manure inputs and is retained in soils or sediments as sorbed, precipitated, or occluded pools.[55] This would create a natural nutrient source for crops and soil organisms, reducing our reliance on finite mineral phosphate fertilizers and supporting a more circular nutrient economy. However, in real farmland, any fertilizer-saving benefit will depend on the coupling between P release, crop root uptake efficiency, and the extent/time scale of P refixation or sorption in soils. Thus, the agronomic outcome will be site-specific and must be validated

https://doi.org/10.1021/acs.est.5c17543
Environ. Sci. Technol. 2026, 60, 13414−13426

alongside plant uptake and soil P buffering capacity to achieve true reduction and efficiency gains. From an application perspective, key challenges include ES stability and persistence in complex media (e.g., oxidation, photodegradation, sorption to minerals/DOM), transport and retention at reactive interfaces, competition with native ligands or shuttles, and potential shifts in microbial community composition and redox balance. Our interfacial-energetics measurements provide a mechanistic basis to address these issues by quantifying how adhesion energy, mineralogy, and solution chemistry control ES-EET efficiency, which can inform ES selection, dosing strategies, and site screening. Although careful management is needed in areas sensitive to eutrophication, strategically applying this process can improve agricultural sustainability by converting stable P reserves into an accessible resource that promotes plant health and a more active soil microbiome. This study is a mechanistic batch incubation and does not fully capture the complexity of natural systems (e.g., competing ions, organic ligands, redox gradients, and spatial heterogeneity). Therefore, the magnitude and persistence of Fe/P mobilization are site-dependent and require mesocosm or field validation. Our results should be interpreted as process-level constraints on ES-enhanced EET rather than direct field-scale quantitative predictions. Future work should integrate site mineralogy, DOM, and hydrologic transport to quantify in situ impacts.

Beyond P mobilization, the thermodynamic framework of ES-enhanced EET elucidated here has broader environmental relevance. The same mechanism that drives Fe(III) reduction and nutrient release could, in principle, be applied to the reductive detoxification of pollutants, such as immobilizing toxic heavy metals (e.g., Cr(VI), U(VI)) or breaking down organic contaminants. However, the practical remediation efficiency may be governed by several factors, including the redox potential of the target contaminant, its binding mode with mineral surfaces, and ambient pH, all of which can influence the electron shuttle-mediated EET process and the resultant reduction outcome. Furthermore, by controlling the oxidation of organic carbon coupled to mineral reduction, EET plays a fundamental role in regulating carbon cycling and storage in oxygen-limited environments. Therefore, our ability to measure, and potentially influence, the energetics of interfacial EET provides a foundational tool. This tool can help us not only optimize nutrient cycles to support ecosystem health but also advance bioremediation strategies and better understand biogeochemical processes relevant to our climate.

■ ASSOCIATED CONTENT

Supporting Information

The Supporting Information is available free of charge at https://pubs.acs.org/doi/10.1021/acs.est.5c17543.

Synthesis and characterization of Fe(III)-phosphate minerals, functionalization of AFM probes with *S. oneidensis* MR-1 cells and riboflavin, SEM imaging of functionalized probes, representative force−distance curves for cell-mineral interactions under varying riboflavin concentrations, kinetics analysis of adhesion forces and Fe(II) production, QNM and stiffness imaging of cell surfaces, electrochemical characterization, determination of dissolved *c*-Cyts concentrations, Raman spectroscopy of intact and ruptured cells, interaction force mapping with RF-functionalized probes, QNM analysis of bacterial nanowires, kinetics of aqueous P release, time-series AFM imaging of mineral dissolution, control experiments with bare probes and filtered cell suspensions, summary tables of adhesion forces, separation distances, and adhesion energies across different minerals and RF concentrations (PDF)

■ AUTHOR INFORMATION

Corresponding Authors

Wenjun Zhang − *College of Resources and Environment, Huazhong Agricultural University, Wuhan 430070, China;* orcid.org/0000-0003-1054-2228; Email: wenjunzhang@mail.hzau.edu.cn

Fangbai Li − *National-Regional Joint Engineering Research Center for Soil Pollution Control and Remediation in South China, Guangdong Key Laboratory of Integrated Agro-Environmental Pollution Control and Management, Institute of Eco-Environmental and Soil Sciences, Guangdong Academy of Sciences, Guangzhou 510650, China;* orcid.org/0000-0001-9027-9313; Email: cefbli@soil.gd.cn

Authors

Yuke Fan − *College of Resources and Environment, Huazhong Agricultural University, Wuhan 430070, China;* orcid.org/0009-0003-4776-2889

Jialin Chi − *National-Regional Joint Engineering Research Center for Soil Pollution Control and Remediation in South China, Guangdong Key Laboratory of Integrated Agro-Environmental Pollution Control and Management, Institute of Eco-Environmental and Soil Sciences, Guangdong Academy of Sciences, Guangzhou 510650, China;* orcid.org/0000-0001-7312-9524

Liping Fang − *National-Regional Joint Engineering Research Center for Soil Pollution Control and Remediation in South China, Guangdong Key Laboratory of Integrated Agro-Environmental Pollution Control and Management, Institute of Eco-Environmental and Soil Sciences, Guangdong Academy of Sciences, Guangzhou 510650, China*

Chonghao Jia − *College of Resources and Environment, Huazhong Agricultural University, Wuhan 430070, China;* orcid.org/0009-0004-6957-0439

Yi Zhang − *College of Resources and Environment, Huazhong Agricultural University, Wuhan 430070, China*

Kai Liu − *National-Regional Joint Engineering Research Center for Soil Pollution Control and Remediation in South China, Guangdong Key Laboratory of Integrated Agro-Environmental Pollution Control and Management, Institute of Eco-Environmental and Soil Sciences, Guangdong Academy of Sciences, Guangzhou 510650, China*

Yundang Wu − *National-Regional Joint Engineering Research Center for Soil Pollution Control and Remediation in South China, Guangdong Key Laboratory of Integrated Agro-Environmental Pollution Control and Management, Institute of Eco-Environmental and Soil Sciences, Guangdong Academy of Sciences, Guangzhou 510650, China;* orcid.org/0000-0003-2996-5407

Xiaokun Li − *College of Resources and Environment, Huazhong Agricultural University, Wuhan 430070, China*

Jianwei Lu − *College of Resources and Environment, Huazhong Agricultural University, Wuhan 430070, China*

https://doi.org/10.1021/acs.est.5c17543
Environ. Sci. Technol. 2026, 60, 13414−13426

Christine V. Putnis − *Institut für Mineralogie, University of Münster, 48149 Münster, Germany; School of Molecular and Life Sciences, Curtin University, Perth 6845, Australia*
Andreas Kappler − *Geomicrobiology, Department of Geosciences, University of Tübingen, Tübingen 72076, Germany;* orcid.org/0000-0002-3558-9500
Lijun Wang − *College of Resources and Environment, Huazhong Agricultural University, Wuhan 430070, China;* orcid.org/0000-0001-7125-9480

Complete contact information is available at: https://pubs.acs.org/10.1021/acs.est.5c17543

Author Contributions

#Y.F. and J.C. contributed equally to this work. Y.F.: Writing—original draft, data curation, formal analysis. J.C.: Writing—review and editing, investigation, formal analysis. L.F.: Investigation, writing—review and editing. C.J. and Y.Z.: Data curation. K.L. and Y.W.: Writing—review and editing. X.L. and J.L.: Investigation, validation. C.V.P. and A.K.: Writing—review and editing. W.Z. and F.L.: Conceptualization, writing—review and editing, supervision, funding acquisition. L.W.: Conceptualization, supervision.

Notes

The authors declare no competing financial interest.

■ ACKNOWLEDGMENTS

This work was financially supported by the National Natural Science Foundation of China (42307014, 42577022, 42321005, U23A2041), the earmarked fund for CARS-12, Major Special Project for the Development of Agricultural Microbial Industry in Hubei Province (NYWSWZX2025-2027-08), the GDAS' Project of Science and Technology Development (2022GDASZH-2022020402-3), and Guangdong Foundation for Program of Science and Technology Research (Grant No. 2023B1212060044).

■ REFERENCES

(1) Rabaey, K.; Rozendal, R. A. Microbial electrosynthesis—revisiting the electrical route for microbial production. *Nat. Rev. Microbiol.* **2010**, *8*, 706−716.
(2) Logan, B. E.; Rossi, R.; Ragab, A.; Saikaly, P. E. Electroactive microorganisms in bioelectrochemical systems. *Nat. Rev. Microbiol.* **2019**, *17*, 307−319.
(3) Jansson, J. K.; Hofmockel, K. S. Soil microbiomes and climate change. *Nat. Rev. Microbiol.* **2020**, *18*, 35−46.
(4) Cologgi, D. L.; Lampa-Pastirk, S.; Speers, A. M.; Kelly, S. D.; Reguera, G. Extracellular reduction of uranium via Geobacter conductive pili as a protective cellular mechanism. *Proc. Natl. Acad. Sci. U.S.A.* **2011**, *108* (37), 15248−15252.
(5) Li, F.-H.; Tang, Q.; Fan, Y.; Li, Y.; Li, J.; Wu, J.; Luo, C.; Sun, H.; Li, W.; Yu, H. Developing a population-state decision system for intelligently reprogramming extracellular electron transfer in *Shewanella oneidensis*. *Proc. Natl. Acad. Sci. U.S.A.* **2020**, *117* (37), 23001−23010.
(6) Wang, H.-B.; Liu, X.-P.; Shu, Y.-C.; Li, G.; Sun, C.-L.; Jones, D. L.; Zhu, Y.-G.; Lin, X.-Y. Molecular composition of exogenous dissolved organic matter regulates dissimilatory iron reduction and carbon emissions in paddy soil. *Environ. Sci. Technol.* **2025**, *59*, 12679−12691.
(7) Schulz, K.; Wisawapipat, W.; Barmettler, K.; Grigg, A. R. C.; Kubeneck, L. J.; Notini, L.; ThomasArrigo, L. K.; Kretzschmar, R. Iron oxyhydroxide transformation in a flooded rice paddy field and the effect of adsorbed phosphate. *Environ. Sci. Technol.* **2024**, *58*, 10601−10610.
(8) Kappler, A.; Bryce, C.; Mansor, M.; Lueder, U.; Byrne, J. M.; Swanner, E. D. An evolving view on biogeochemical cycling of iron. *Nat. Rev. Microbiol.* **2021**, *19*, 360−374.
(9) Kappler, A.; Thompson, A.; Mansor, M. Impact of biogenic magnetite formation and transformation on biogeochemical cycles. *Elements* **2023**, *19*, 222−227.
(10) Chen, G.; Bai, Y.; Zeng, R. J.; Qin, L. Effects of different metabolic pathways and environmental parameters on Cr isotope fractionation during Cr(VI) reduction by extremely thermophilic bacteria. *Geochim. Cosmochim. Acta* **2019**, *256*, 135−146.
(11) Shi, L.; Dong, H.; Reguera, G.; Beyenal, H.; Lu, A.; Liu, J.; Yu, H.-Q.; Fredrickson, J. K. Extracellular electron transfer mechanisms between microorganisms and minerals. *Nat. Rev. Microbiol.* **2016**, *14*, 651−662.
(12) Melton, E. D.; Swanner, E. D.; Behrens, S.; Schmidt, C.; Kappler, A. The interplay of microbially mediated and abiotic reactions in the biogeochemical Fe cycle. *Nat. Rev. Microbiol.* **2014**, *12*, 797−808.
(13) Cisternas, I. S.; Salazar, J. C.; García-Angulo, V. A. Overview on the bacterial iron-riboflavin metabolic axis. *Front. Microbiol.* **2018**, *9*, No. 1478.
(14) Shi, Z.; Zachara, J. M.; Shi, L.; Wang, Z.; Moore, D. A.; Kennedy, D. W.; Fredrickson, J. K. Redox reactions of reduced flavin mononucleotide (FMN), riboflavin (RBF), and anthraquinone-2,6-disulfonate (AQDS) with ferrihydrite and lepidocrocite. *Environ. Sci. Technol.* **2012**, *46*, 11644−11652.
(15) Wu, Y.; Liu, T.; Li, X.; Li, F. Exogenous electron shuttle-mediated extracellular electron transfer of *Shewanella putrefaciens* 200: Electrochemical parameters and thermodynamics. *Environ. Sci. Technol.* **2014**, *48*, 9306−9314.
(16) Aeppli, M.; Giroud, S.; Vranic, S.; Voegelin, A.; Hofstetter, T. B.; Sander, M. Thermodynamic controls on rates of iron oxide reduction by extracellular electron shuttles. *Proc. Natl. Acad. Sci. U.S.A.* **2022**, *119*, No. e2115629119.
(17) Yan, W.; Wang, H.; Jing, C. Adhesion of *Shewanella oneidensis* MR-1 to goethite: A two-dimensional correlation spectroscopic study. *Environ. Sci. Technol.* **2016**, *50*, 4343−4349.
(18) Han, J.-C.; Chen, G.-J.; Qin, L.-P.; Mu, Y. Metal respiratory pathway-independent Cr isotope fractionation during Cr(VI) reduction by *Shewanella oneidensis* MR-1. *Environ. Sci. Technol. Lett.* **2017**, *4*, 500−504.
(19) Min, D.; Cheng, L.; Zhang, F.; Huang, X.-N.; Li, D.-B.; Liu, D.-F.; Lau, T.-C.; Mu, Y.; Yu, H.-Q. Enhancing extracellular electron transfer of *Shewanella oneidensis* MR-1 through coupling improved flavin synthesis and metal-reducing conduit for pollutant degradation. *Environ. Sci. Technol.* **2017**, *51*, 5082−5089.
(20) Wu, Y.; Zhu, X.; Wang, X.; Lin, Z.; Reinfelder, J. R.; Li, F.; Liu, T. A new electron shuttling pathway mediated by lipophilic phenoxazine via the interaction with periplasmic and inner membrane proteins of *Shewanella oneidensis* MR-1. *Environ. Sci. Technol.* **2023**, *57*, 2636−2646.
(21) Tokunou, Y.; Tongu, H.; Kogure, Y.; Okamoto, A.; Toyofuku, M.; Nomura, N. Colony-based electrochemistry reveals electron conduction mechanisms mediated by cytochromes and flavins in *Shewanella oneidensis*. *Environ. Sci. Technol.* **2024**, *58*, 4670−4679.
(22) Liu, T.; Luo, X.; Wu, Y.; Reinfelder, J. R.; Yuan, X.; Li, X.; Chen, D.; Li, F. Extracellular electron shuttling mediated by soluble *c*-type cytochromes produced by *Shewanella oneidensis* MR-1. *Environ. Sci. Technol.* **2020**, *54*, 10577−10587.
(23) Chi, J.; Liu, K.; Wu, S.; Zhang, W.; Shi, Q.; Fang, L.; Li, F. Dual-ligand-driven dark reactive oxygen species generation on iron oxyhydroxides: Implications for environmental remediation. *Environ. Sci. Technol.* **2024**, *58*, 20751−20760.
(24) Wang, H.; Zhang, N.; Ma, H.-Y.; Chen, X. DFT study of copper-based single-atom alloy for conversion of carbon dioxide to formic acid. *ACS Appl. Nano Mater.* **2024**, *7*, 21717−21727.
(25) Tsai, H.-C.; Hsieh, Y.-C.; Yu, T. H.; Lee, Y.-J.; Wu, Y.-H.; Merinov, B. V.; Wu, P.-W.; Chen, S.-Y.; Adzic, R. R.; Goddard, W. A. DFT study of oxygen reduction reaction on Os/Pt core−shell

catalysts validated by electrochemical experiment. *ACS Catal.* **2015**, *5*, 1568−1580.
(26) Beaussart, A.; El-Kirat-Chatel, S.; Sullan, R. M. A.; Alsteens, D.; Herman, P.; Derclaye, S.; Dufrêne, Y. F. Quantifying the forces guiding microbial cell adhesion using single-cell force spectroscopy. *Nat. Protoc.* **2014**, *9*, 1049−1055.
(27) von Canstein, H.; Ogawa, J.; Shimizu, S.; Lloyd Jonathan, R. Secretion of flavins by shewanella species and their role in extracellular electron transfer. *Appl. Environ. Microbiol.* **2008**, *74* (3), 615−623.
(28) Marsili, E.; Baron, D. B.; Shikhare, I. D.; Coursolle, D.; Gralnick, J. A.; Bond, D. R. Shewanella secretes flavins that mediate extracellular electron transfer. *Proc. Natl. Acad. Sci. U.S.A.* **2008**, *105* (10), 3968−3973.
(29) Friddle, R. W.; Noy, A.; De Yoreo, J. J. Interpreting the widespread nonlinear force spectra of intermolecular bonds. *Proc. Natl. Acad. Sci. U.S.A.* **2012**, *109*, 13573−13578.
(30) Gao, K.; Zhu, H.; Zhou, W.; Hu, S.; Zhang, B.; Ding, Z.; Liu, C. Effect of phosphate on ferrihydrite transformation and the associated arsenic behavior mediated by sulfate-reducing bacterium. *J. Hazard. Mater.* **2023**, *448*, No. 130863.
(31) Luo, X.; Wu, Y.; Liu, T.; Li, F.; Li, X.; Chen, D.; Wang, Y. Quantifying redox dynamics of c-type cytochromes in a living cell suspension of dissimilatory metal-reducing bacteria. *Anal. Sci.* **2019**, *35*, 315−321.
(32) Hansma, H. G.; Hoh, J. H. Biomolecular imaging with the atomic force microscope. *Annu. Rev. Biophys. Biomol. Struct.* **1994**, *23*, 115−140.
(33) Kim, H.; Witt, H.; Oswald, T. A.; Tarantola, M. Adhesion of epithelial cells to PNIPAm treated surfaces for temperature-controlled cell-sheet harvesting. *ACS Appl. Mater. Interfaces.* **2020**, *12*, 33516−33529.
(34) Newcomb, C. J.; Qafoku, N. P.; Grate, J. W.; Bailey, V. L.; De Yoreo, J. J. Developing a molecular picture of soil organic matter−mineral interactions by quantifying organo−mineral binding. *Nat. Commun.* **2017**, *8*, No. 396, DOI: 10.1038/s41467-017-00407-9.
(35) Knoops, B.; Becker, S.; Poncin, M. A.; Glibert, J.; Derclaye, S.; Clippe, A.; Alsteens, D. Specific interactions measured by AFM on living cells between Peroxiredoxin-5 and TLR4: Relevance for mechanisms of innate immunity. *Cell Chem. Biol.* **2018**, *25*, 550−559.e3.
(36) Brown, A. R.; Molinas, M.; Roebbert, Y.; Sato, A.; Abe, M.; Weyer, S.; Bernier-Latmani, R. Electron flux is a key determinant of uranium isotope fractionation during bacterial reduction. *Commun. Earth Environ.* **2023**, *4*, No. 329.
(37) Meyer, E. E.; Rosenberg, K. J.; Israelachvili, J. Recent progress in understanding hydrophobic interactions. *Proc. Natl. Acad. Sci. U.S.A.* **2006**, *103*, 15739−15746.
(38) Li, S.; Zheng, M.; Wu, S.; Xue, Y.; Liu, Y.; Wang, C.; Huang, X. The impact of ultrasonic treatment on activity of ammonia-oxidizing bacteria and nitrite-oxidizing bacteria in activated sludge. *Front. Environ. Sci. Eng.* **2019**, *13*, No. 82.
(39) Li, R.; Tiedje, J. M.; Chiu, C.; Worden, R. M. Soluble electron shuttles can mediate energy taxis toward insoluble electron acceptors. *Environ. Sci. Technol.* **2012**, *46*, 2813−2820.
(40) Okamoto, A.; Hashimoto, K.; Nealson, K. H.; Nakamura, R. Rate enhancement of bacterial extracellular electron transport involves bound flavin semiquinones. *Proc. Natl. Acad. Sci. U.S.A.* **2013**, *110*, 7856−7861.
(41) Light, S. H.; Su, L.; Rivera-Lugo, R.; Cornejo, J. A.; Louie, A.; Iavarone, A. T.; Ajo-Franklin, C. M.; Portnoy, D. A. A flavin-based extracellular electron transfer mechanism in diverse Gram-positive bacteria. *Nature* **2018**, *562*, 140−144.
(42) Subramanian, P.; Pirbadian, S.; El-Naggar, M. Y.; Jensen, G. J. Ultrastructure of *Shewanella oneidensis* MR-1 nanowires revealed by electron cryotomography. *Proc. Natl. Acad. Sci. U.S.A.* **2018**, *115* (14), E3246−E3255.
(43) Pirbadian, S.; Barchinger, S. E.; Leung, K. M.; Byun, H. S.; Jangir, Y.; Bouhenni, R. A.; Reed, S. B.; Romine, M. F.; Saffarini, D. A.; Shi, L.; Gorby, Y. A.; Golbeck, J. H.; El-Naggar, M. Y. *Shewanella oneidensis* MR-1 nanowires are outer membrane and periplasmic extensions of the extracellular electron transport components. *Proc. Natl. Acad. Sci. U.S.A.* **2014**, *111*, 12883−12888.
(44) Yuan, Y.; Li, L.; Zhou, S. Axial ligation of heme in c-type cytochromes of living *Shewanella oneidensis*: A new insight into enhanced extracellular electron transfer. *ChemElectroChem* **2015**, *2*, 1672−1677.
(45) Xu, S.; Jangir, Y.; El-Naggar, M. Y. Disentangling the roles of free and cytochrome-bound flavins in extracellular electron transport from *Shewanella oneidensis* MR-1. *Electrochim. Acta* **2016**, *198*, 49−55.
(46) Gorby, Y. A.; Yanina, S.; McLean, J. S.; Rosso, K. M.; Moyles, D.; Dohnalkova, A.; Beveridge, T. J.; Chang, I. S.; Kim, B. H.; Kim, K. S.; Culley, D. E.; Reed, S. B.; Romine, M. F.; Saffarini, D. A.; Hill, E. A.; Shi, L.; Elias, D. A.; Kennedy, D. W.; Pinchuk, G.; Watanabe, K.; Ishii, S. I.; Logan, B.; Nealson, K. H.; Fredrickson, J. K. Electrically conductive bacterial nanowires produced by *Shewanella oneidensis* strain MR-1 and other microorganisms. *Proc. Natl. Acad. Sci. U.S.A.* **2006**, *103*, 11358−11363.
(47) El-Naggar, M. Y.; Wanger, G.; Leung, K. M.; Yuzvinsky, T. D.; Southam, G.; Yang, J.; Lau, W. M.; Nealson, K. H.; Gorby, Y. A. Electrical transport along bacterial nanowires from *Shewanella oneidensis* MR-1. *Proc. Natl. Acad. Sci. U.S.A.* **2010**, *107*, 18127−18131.
(48) Eltohamy, K. M.; Menezes-Blackburn, D.; Klumpp, E.; Liu, C.; Jin, J.; Xing, C.; Lu, Y.; Liang, X. Microbially induced soil colloidal phosphorus mobilization under anoxic conditions. *Environ. Sci. Technol.* **2024**, *58*, 7554−7566.
(49) Xue, Y.; Loranger, M. E. W.; Jia, Y.; Andoy, N. M. O.; Moeder, W.; Yoshioka, K.; Sullan, R. M. A. Single-cell force spectroscopy uncovers root zone- and bacteria-specific interactions. *Angew. Chem. Int. Ed* **2025**, *64*, No. e202419510.
(50) Lopes, C. S.; Curty, J.; Carvalho, F. A.; Hernández-Machado, A.; Kinoshita, K.; Santos, N. C.; Travasso, R. D. M. A mathematical model of fibrinogen-mediated erythrocyte−erythrocyte adhesion. *Commun. Biol.* **2023**, *6*, No. 192.
(51) Spoerri, P. M.; Strohmeyer, N.; Sun, Z.; Fässler, R.; Müller, D. J. Protease-activated receptor signalling initiates $\alpha 5\beta 1$-integrin-mediated adhesion in non-haematopoietic cells. *Nat. Mater.* **2020**, *19*, 218−226.
(52) Müller, D. J.; Dumitru, A. C.; Giudice, C. L.; Gaub, H. E.; Hinterdorfer, P.; Hummer, G.; De Yoreo, J. J.; Dufrêne, Y. F.; Alsteens, D. Atomic force microscopy-based force spectroscopy and multiparametric imaging of biomolecular and cellular systems. *Chem. Rev.* **2021**, *121*, 11701−11725.
(53) Dupres, V.; Menozzi, F. D.; Locht, C.; Clare, B. H.; Abbott, N. L.; Cuenot, S.; Bompard, C.; Raze, D.; Dufrêne, Y. F. Nanoscale mapping and functional analysis of individual adhesins on living bacteria. *Nat. Methods* **2005**, *2*, 515−520.
(54) Alsteens, D.; Newton, R.; Schubert, R.; Martinez-Martin, D.; Delguste, M.; Roska, B.; Müller, D. J. Nanomechanical mapping of first binding steps of a virus to animal cells. *Nat. Nanotechnol.* **2017**, *12*, 177−183.
(55) Wang, Y.; Chen, H.; Zhao, H.; Gao, J.; Su, W.; Zhu, M.; Turner, B. L.; Peñuelas, J.; Whalen, J. K.; Wang, Y.; Wang, L.; Yan, X.; Zhou, D.; Pokharel, P.; Wang, S.; Yuan, Z.; Zhu, Y.-G. Unlocking legacy phosphorus sustains yields and reduces emissions with paddy-upland rotation cultivation. *One Earth* **2025**, *8* (12), No. 101449.